

# Laminated Polymer-Encapsulated Halide Perovskite Photoconductors

Bas A. H. Huisman, Camilla Bordoni, Andrea Ciavatti, Michele Sessolo,\* Beatrice Fraboni, and Henk J. Bolink\*

Herein, a simple, solvent-free method to fabricate polymer-encapsulated halide perovskite photoconductors is described. Dry mechanochemical synthesis is used to prepare CsPbBr<sub>3</sub> in the presence of poly(butyl methacrylate) (PBMA). The resulting composite powder is then heated and pressed into a free-standing disk with a thickness controlled by a metallic spacer ring. The disk can be laminated on a glass substrate patterned with interdigitated electrodes, resulting in a planar photoconductor device. The best photoconductive performance is obtained for disks that consist of 75 wt.% CsPbBr<sub>3</sub> in PBMA, reaching a detectivity of  $\approx 2 \times 10^{11}$  Jones. Moreover, by adjusting the thickness of the disk, narrowband detectors can be obtained due to charge collection narrowing. Depending on the thickness of the pressed disk, the position and width of the detectivity peak can be tuned. At last, the disks are tested as possible absorber materials for X-ray detectors, where low detection limit, and fast and linear response are measured for perovskite-polymer disks with 50 wt.% perovskite content. This work shows a simple and versatile approach toward the fabrication of halide perovskite photodetectors, which can be carried out in air and without the use of solvents.

Photodiodes include electron and hole transport layers that allow for current flow only in one bias direction, while the layout of a photoconductor is simpler, consisting of a metal-semiconductor-metal structure.<sup>[4]</sup> The simple structure of a photoconductor allows the use of simple device designs such as planar layouts. Photoconductors can exhibit high photocurrents due to the gain effect, resulting in high responsivity.<sup>[5]</sup> The semiconducting (light-sensitive) material employed determines to a large extent the characteristics of photoconductors, such as their response speed and spectral sensitivity.<sup>[6]</sup> Therefore, it is important to use the correct semiconductor for different applications.

Metal halide perovskites (herein simply perovskites) are widely studied semiconductors, due to their favorable optoelectronic properties, simple processing, and easy tunability of their properties.<sup>[7–9]</sup> As a result, high-performing photodetectors have been demonstrated using perovskites.<sup>[4,10–13]</sup> However, several

challenges remain regarding stability, the realization of filterless narrowband photodetectors, as well as very broadband photodetectors. Additionally, processing methods compatible with large-scale production in an industrial environment are still missing.<sup>[4,10,12,13]</sup> Solvent-free, low-cost, simple production processes are advantageous to bring some of these devices closer to the market.


Mechanochemical synthesis has shown great potential for the preparation of perovskite powders.<sup>[14–20]</sup> The perovskite is simply obtained by grinding the different precursors in the desired stoichiometry. This process is scalable, solvent-free, and offers facile stoichiometric control so that different and complex perovskite compositions can be easily obtained.<sup>[21–23]</sup>

In a previous study, we used mechanochemical synthesis for the preparation of perovskite-polymer composites for color converters.<sup>[24]</sup> Briefly, a perovskite powder was prepared by mechanochemical synthesis and then mixed with a commercial thermoplastic polymer through an additional ball-milling step. Polymers have been used in perovskite devices often as an additive, passivating agent, or complementary absorber layer.<sup>[25–27]</sup> The presence of the thermoplastic polymer in the perovskite-polymer composite allows these powders to be pressed into thin disks. This was done by inserting the composite powder into a

## 1. Introduction

Photodetectors are widely used for optical communications, imaging, and biomedical sensing.<sup>[1–3]</sup> In short, a photodetector converts an optical signal to an electronic signal. Two types of photodetectors exist, photodiodes and photoconductors.

B. A. H. Huisman, M. Sessolo, H. J. Bolink  
Instituto de Ciencia Molecular  
Universidad de Valencia  
C/ Catedrático J. Beltrán 2, Paterna 46980, Spain  
E-mail: michele.sessolo@uv.es; henk.bolink@uv.es  
C. Bordoni, A. Ciavatti, B. Fraboni  
Department of Physics and Astronomy  
Alma Mater Studiorum – University of Bologna  
Viale C. Berti-Pichat 6/2, Bologna 40127, Italy

 The ORCID identification number(s) for the author(s) of this article can be found under <https://doi.org/10.1002/adfm.202308844>

© 2023 The Authors. Advanced Functional Materials published by Wiley-VCH GmbH. This is an open access article under the terms of the Creative Commons Attribution License, which permits use, distribution and reproduction in any medium, provided the original work is properly cited.

DOI: 10.1002/adfm.202308844

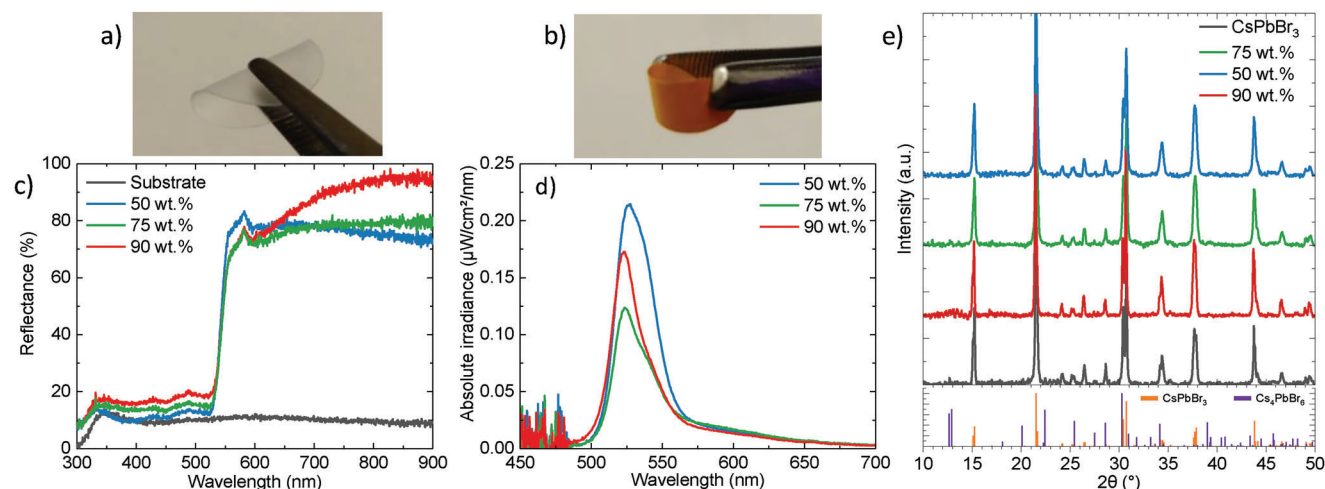


**Figure 1.** a) Photographs of a PBMA disk and b) a disk of 75 wt.% CsPbBr<sub>3</sub> in PBMA. c) Reflectance spectra of disks with different concentrations of CsPbBr<sub>3</sub> laminated on a glass substrate (black reference). d) Photoluminescence spectra of the different disks, excited by a 405 nm laser. e) XRD pattern of the initial ball-milled CsPbBr<sub>3</sub> powder and the patterns of the disks with different wt.% of CsPbBr<sub>3</sub> in PBMA. In the lower section, the reference patterns of CsPbBr<sub>3</sub> (COD ID: 4510745) and Cs<sub>4</sub>PbBr<sub>6</sub> (COD ID: 1538416) are reported.

pre-heated mold and applying pressure up to 1.5 metric tons for 10 s. The thickness of the disks was fixed by the thickness of the spacer rings placed in the mold. The disks were characterized only on their optical properties as no electrodes were placed on them.

Here we demonstrate perovskite-polymer composites that can be used as an absorber layer in photoconductors. The disks, consisting of the perovskite CsPbBr<sub>3</sub> and poly(butyl methacrylate) (PBMA), are simply adhered by hot roll lamination on a glass substrate containing an interdigitated array of indium tin oxide (ITO) electrodes. With this simple procedure, lateral photoconductors are readily obtained. Devices with a detectivity around  $2 \times 10^{11}$  Jones are produced when the disk is illuminated through the glass, showing that the polymer-perovskite disks can be a suitable candidate as a photoconductive material. Furthermore, the process enables to easily achieve thick disks, which can be used as filterless narrowband photoconductors. This proof of concept is the first step towards the facile fabrication of more complex perovskite-polymer photoconductors as well as narrowband photoconductors.

## 2. Results and Discussion

The inorganic halide perovskite CsPbBr<sub>3</sub> was selected as the absorber material for the photoconductor due to its high thermal stability and good semiconducting properties. The perovskite was mechano-synthesized by adding a stoichiometric ratio of cesium bromide and lead bromide in a zirconium ball jar of 10 mL followed by ball milling at a frequency of 30 Hz for 5 min with a Rensch MM400.<sup>[28]</sup> After the formation of the perovskite, PBMA in powder form was added to obtain the desired polymer-perovskite ratio and the mixture was ball-milled for an additional 3 min at the same frequency to obtain a thoroughly mixed polymer-perovskite composite. PBMA was selected due to its mechanical stability (Figure 1a) and adhesive properties with the substrate when laminating (see Table S1, Supporting Information for a list of polymers that were tested and their properties in the compos-

ite). Furthermore, PBMA absorbs only in the UV region (< 300 nm) and therefore has a very low parasitic absorption (see Figure S1, Supporting Information), comparable to that of the glass substrates used in the devices. The perovskite-polymer composite is heated up to 100 °C and pressed for 1 s at 2 metric tons using a spacer ring to obtain a 100 μm thick mechanical stable disk (Figure 1b). Once the disks are formed, they are laminated on a glass substrate containing a pre-patterned interdigitated array of ITO electrodes using a roll-to-roll laminator set at a temperature of 100 °C. The spacing between the ITO electrodes is 40 μm. For more information, see the Experimental Section.

Initially, the effect of the perovskite content on the physical properties of the composite was studied. In Figure 1c,d, the optical properties of the disk with different perovskite loading (expressed in weight percentages, wt.%) in PBMA are reported. From the reflectance measurements in Figure 1c, it is visible that all disks have a cut-off around 530 nm, which is in agreement with the bandgap of CsPbBr<sub>3</sub>.<sup>[29]</sup> In Figure 1d the photoluminescence (PL) spectra of the different disks, when excited by a 405 nm laser are shown. The spectra are very similar independent of the perovskite concentration, although there is an optimum in the intensity for the disk containing 50 wt.%. This is most likely due to a more complete encapsulation of the CsPbBr<sub>3</sub> regions as the amount of PBMA is larger in this composite. For all the disks the most intense PL peak is at  $\approx 525 \pm 2$  nm, and there is a secondary PL component visible at lower energy around 540 nm. The lower-energy emission is typical for an orthorhombic bulk CsPbBr<sub>3</sub> perovskite, whereas the PL peak at 525 nm is explained by weakly-quantum-confined (i.e., “nano”) CsPbBr<sub>3</sub> particles.<sup>[28,29]</sup> Note that there seems not to be any apparent chemical interaction between the polymer and the perovskite, as from X-ray photoelectron spectroscopy (Figure S2, Supporting Information), the peak shapes and position agree with the presence of the isolated perovskite and polymer, with no chemical shift due to their interaction.

The X-ray diffraction (XRD) patterns of disks with different perovskite loading in PBMA are reported, together with the XRD

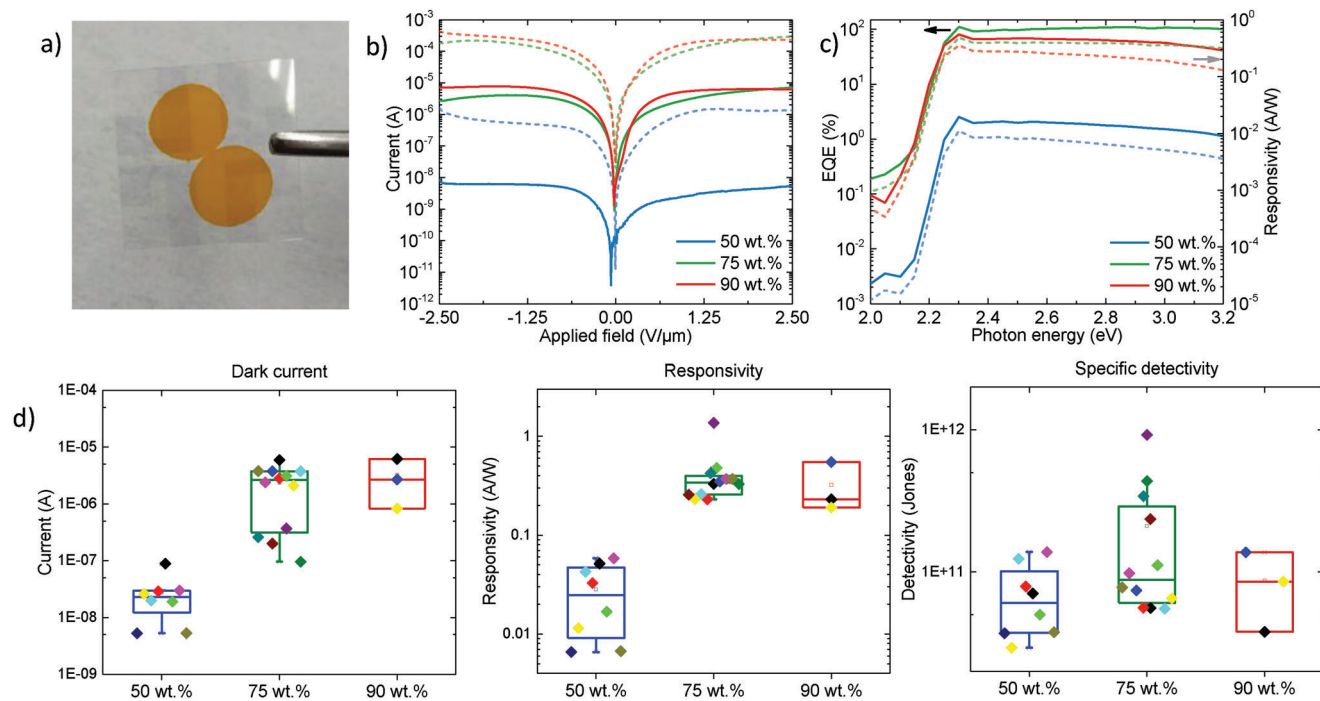


**Figure 2.** a) Photograph of a device with two disks adhered on a substrate with interdigitated electrodes. b)  $I$ - $V$  curves under dark conditions (solid lines) and under white light illumination (dashed lines). c) The solid lines represent the EQE of the devices with different weight percentages of perovskite with respect to PBMA under an applied field of  $2.5 \text{ V } \mu\text{m}^{-1}$ . The dashed lines are the corresponding responsivity. d) Statistics of device parameters for several photoconductors with different perovskite content at an applied field of  $2.5 \text{ V } \mu\text{m}^{-1}$ . Every colored dot represents a different device.

pattern of the pure as-prepared  $\text{CsPbBr}_3$  powder in Figure 1e. The pristine  $\text{CsPbBr}_3$  powder shows a diffraction pattern compatible with that of an orthorhombic phase, as expected at room temperature.<sup>[30,31]</sup> This diffraction pattern is maintained when adding the PBMA to the perovskite powder and when these powders are pressed into thin disks with different perovskite concentrations. Both the XRD and PL measurements are consistent with the formation of polycrystalline orthorhombic  $\text{CsPbBr}_3$  perovskite in the composite disks.

The disks laminated on planar interdigitated ITO electrodes (Figure 2a) are then characterized for their photoconductive properties. To characterize the devices, we measured the current versus voltage ( $I$ - $V$ ) curves in dark conditions and under illumination, as well as the external quantum efficiency (EQE). First,  $I$ - $V$  curves are measured in dark conditions and under white light illumination ( $100 \text{ mW cm}^{-2}$ ) for the photoconductors with disks containing perovskite/PBMA composites with different perovskite contents (Figure 2b). The voltage is swept from negative to positive bias. Interestingly, the dark current increases with increasing perovskite content in the composite material. This might be related to a better charge percolation with higher perovskite content, or a transition from hopping transport between the perovskite particles to bulk semiconductivity.<sup>[32]</sup> Under illumination, the photoconductor with 75 and 90 wt.% perovskite shows the highest photocurrent.

In Figure 2c the EQE of the photoconductors with different content of  $\text{CsPbBr}_3$  in PBMA, recorded under an applied field at  $2.5 \text{ V } \mu\text{m}^{-1}$  ( $100 \text{ V}$  applied bias), are reported. All devices show a cut-off around  $2.3 \text{ eV}$ , which agrees with the bandgap of

$\text{CsPbBr}_3$ .<sup>[33]</sup> As expected from the photocurrent measurements, the photoconductor with 75 and 90 wt.%  $\text{CsPbBr}_3$  in PBMA shows also the highest EQE, where the EQE decreases when decreasing the perovskite concentration to 50 wt.%. For the photoconductor with 75 wt.% perovskite in PBMA, the EQE exceeds 100% in certain regions, a consequence of the gain mechanism typically observed in photoconductors.<sup>[5]</sup> Besides the EQE, the responsivity of the devices is also displayed in Figure 2c. The responsivity is similarly constant over the vis-UV range, which is desirable for any photodetector and not always observed in the case of perovskite photoconductors.<sup>[34,35]</sup>

To evaluate the reproducibility of the processing method reported here, the device configurations with different perovskite content were repeated several times with different batches of ball-milled powder. In Figure 2d, the statistics of the different devices are plotted for the dark current, responsivity, and detectivity, respectively. Although the 90 wt.% devices observed similar performances as the 75 wt.% devices, the yield of working devices for 90 wt.% is very low (< 20%). In Figure S3, Supporting Information the  $I$ - $V$  curves under dark and illumination for multiple devices with 90 wt.% content are plotted, highlighting the spreading among them and the low photocurrent in most cases. The low yield of working devices is likely due to bad lamination of the disk on the substrate or due to cracks in the film, because of the small amount of PBMA. Due to the low reproducibility of the 90 wt.% devices and the fact that the 75 wt.% show similar performance, the 90 wt.% devices were not analyzed for their time response. Observing, the devices with 50 and 75 wt.% perovskite content, small differences in the dark current can be observed at

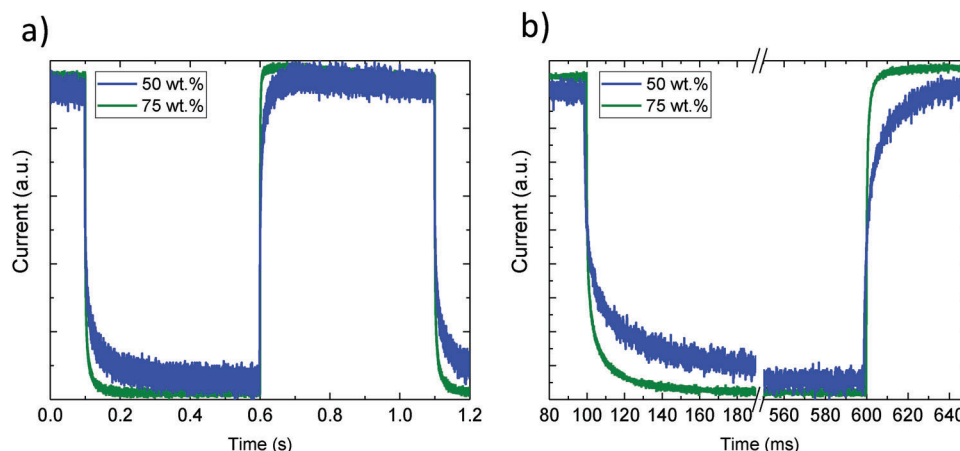


**Figure 3.** Response devices (50 and 75 wt.% perovskite) when excited by a pulsed laser of 1 Hz and an excitation wavelength of 405 nm. a) Response of the devices in a time scale where the whole on and off state is visible. b) Cropped figure of the response of the devices, where the fall and rise response is visualized.

different wt.% for the different devices, but overall most devices have a dark current mean value of  $2.8 \times 10^{-8}$  A for the 50 wt.% devices, and of  $2.3 \times 10^{-6}$  A for the 75 wt.% devices. The mean value of the responsivity ( $R$ ) of the 50 wt.% photoconductor ( $0.028 \text{ A W}^{-1}$ ) is approximately one order of magnitude lower than the mean value of  $R$  for the device with 75 wt.% perovskite ( $0.42 \text{ A/W}$ ). Furthermore, the responsivity of the photoconductor with 75 wt.% perovskite seems more consistent, with a much narrower data distribution. Finally, from the dark current and the responsivity data, an estimation of the specific detectivity ( $D^*$ ) of the different devices can be calculated using Equation (S1), Supporting Information. This resulted in  $D^*$  with a mean value of  $7 \times 10^{10}$  Jones for the photoconductor with 50 wt.% perovskite. Increasing the perovskite content to 75 wt.% leads to a mean value of  $2 \times 10^{11}$  Jones. Also, for the 75 wt.% perovskite composite, another batch of eight devices was measured with a lower applied field of  $1.25 \text{ V } \mu\text{m}^{-1}$ , resulting in a mean value of  $10^{11}$  Jones (see Figure S4, Supporting Information). The difference in dark currents over the devices is likely due to different ambient conditions the powders are pressed during half a year of processing devices. It is known that humidity can affect the semiconducting properties of  $\text{CsPbBr}_3$ . Therefore, to enhance reproducibility it is suggested to press in a controlled environment, like a humidity chamber. Overall, the devices showed very promising reproducibility despite the simple fabrication in ambient air.

Another important figure of merit for photodetectors is their response time. The rise or fall time is the time needed to change to 90% of the final value of the signal. To calculate the response time, a pulsed laser with a wavelength of 405 nm at a frequency of 1 Hz excites the device and the response of the device is measured. In Figure 3 the response of a 75 wt.% perovskite device is reported, showing a rise time of 1.78 ms and a fall time of 8.63 ms, at an applied field of  $2.5 \text{ V } \mu\text{m}^{-1}$ . In the same figure, the response of a 50 wt.% perovskite device is displayed at an applied field of  $2.5 \text{ V } \mu\text{m}^{-1}$ , where a rise time of 13.5 ms and a fall time of 28.9 ms were measured. The increase in rise and fall time with a lower amount of perovskite can be related to the lower conductivity of the 50 wt.% perovskite devices (Figure 2b). Also, in general, a higher applied field results in a faster response time for the de-

vice due to a higher drift velocity.<sup>[36,37]</sup> Indeed, when measuring a 75 wt.% perovskite device where a lower field of  $1.25 \text{ V } \mu\text{m}^{-1}$  is applied the rise and fall time were increased to 12.2 and 55.9 ms, respectively.

The process presented here allows us to tune the thickness of the disks by simply changing the height of the spacer rings, from tens to hundreds of micrometers. Such thick films can be used for the detection of ionizing radiation, or to obtain narrowband photodetectors leveraging the process known as charge column narrowing. In a thick semiconductor, the shorter wavelengths are quantitatively absorbed in the vicinity of the surface, and the photogenerated charges will recombine before reaching the electrodes. On the other hand, low-energy photons close to the bandgap of the semiconductor are absorbed within the volume of the material, hence creating charge carriers closer to the contact which leads to the photocurrent. In this way, it is possible to make a filterless narrow-band photodetector with only one thick absorber layer.<sup>[38,39]</sup> To test for this effect on our perovskite-polymer composites, a series of devices with increasing disk thickness was prepared, and characterized with illumination from the top of the perovskite composite disk (opposite side as of the ITO electrodes). The specific detectivity spectra of devices with increasing disk thickness are reported in Figure 4, both in linear and semi-log scales. We observed a narrowband response in all cases, although thinner disks ( $25 \mu\text{m}$ ) were found to lead to higher specific detectivity. The thicker the disk, the more effective charge collection narrowing, and red-shifting of the spectral response peak. However, by increasing the disk thickness,  $D^*$  was found to decrease accordingly, as fewer low-energy photons can reach the vicinity of the bottom interdigitated ITO contacts. In Figure S5, Supporting Information, the corresponding detectivity of different devices, with a thickness of  $25 \mu\text{m}$  when illuminated at the perovskite side at a field of  $2.5 \text{ V } \mu\text{m}^{-1}$ , is shown. As can be observed a peak at 555 nm is observed and maintained for all devices, corresponding to a narrow-band photodetector. The full width at half maximum FWHM of the peak is as narrow as 15 nm, which is remarkable for such a simple device layout. The specific detectivity of the narrow-band detectors is in the range of  $1$  to  $7 \times 10^9$  Jones.



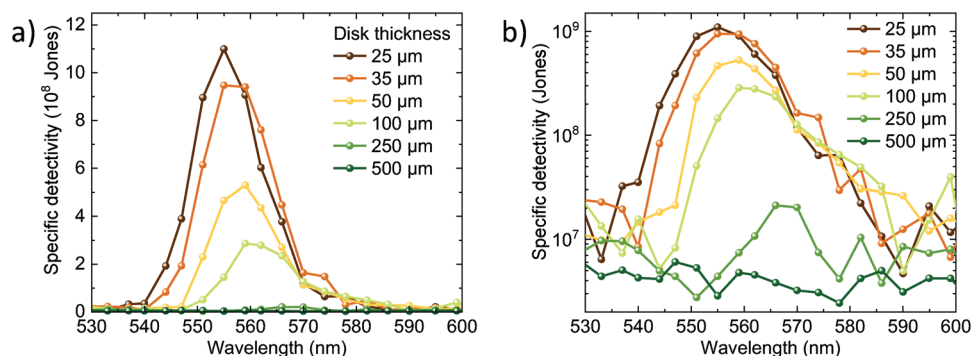


**Figure 4.** Narrowband photodetectors are obtained by illuminating the devices on the opposite side of the ITO electrodes. a) Specific detectivity of 75 wt.% perovskite devices with different thicknesses, collected at  $2.5 \text{ V } \mu\text{m}^{-1}$ . The same dataset is plotted in (b) but represented in a semi-log scale.

In the above-described experiments, the devices are tested on their photoconductive properties with wavelengths in the visible range. As mentioned earlier, the preparation method allows the production of easily thick disks, which makes them also interesting as active materials for the detection of ionizing radiation, such as X-rays. Hence, the devices with a thickness of 100  $\mu\text{m}$  thick disks were tested under irradiation with 150 kVp photons at different doses. Initially, the optimal bias is identified by looking at the current/on/off ratio at different applied voltages, at a dose of  $1480 \mu\text{G s}^{-1}$  (Figure S6, Supporting Information). The on/off ratio is maximized at an applied field of  $0.5 \text{ V } \mu\text{m}^{-1}$  (20 V), and it does not increase further for higher voltages. To determine the linearity of the devices and their sensitivity, the devices were irradiated at different dose rates and the output signal was measured. The three disks with different weight percentages of  $\text{CsPbBr}_3$  have a sensitivity of 1.0, 3.7, and  $1.0 \mu\text{C Gy}^{-1}$  for the 50, 75, and 90 wt.% devices respectively. Although the highest sensi-

tivity is measured for the devices with disks at 75 wt.% perovskite content, the current was observed to drift substantially during the measurements, hindering a reliable characterization (see Figure S7, Supporting Information). Again, the devices with disks at 90 wt.% perovskite content showed a low yield. In spite of their moderate sensitivity, for the 50 wt.% perovskite-polymer disks the output signal was found to be stable over time, with a fast and linear response to different X-ray doses (Figure 5a,b). For the 50 wt.% perovskite disks, additional measurements with lower doses are performed to obtain the limit of detection, which was found to be  $3 \pm 1.1 \mu\text{G s}^{-1}$  (Figure 5b,c). It is worth noting that both the device sensitivity and limit of detection are likely limited by the charge diffusion length in the perovskite/polymer composite, as in the lateral device configuration used here not the full volume of the disks contributes to the photocurrent. Indeed, among the  $\approx 1.8\%$  absorbed radiation in a 100  $\mu\text{m}$  thick perovskite polymer composite, the majority is absorbed far from the bottom electrodes.

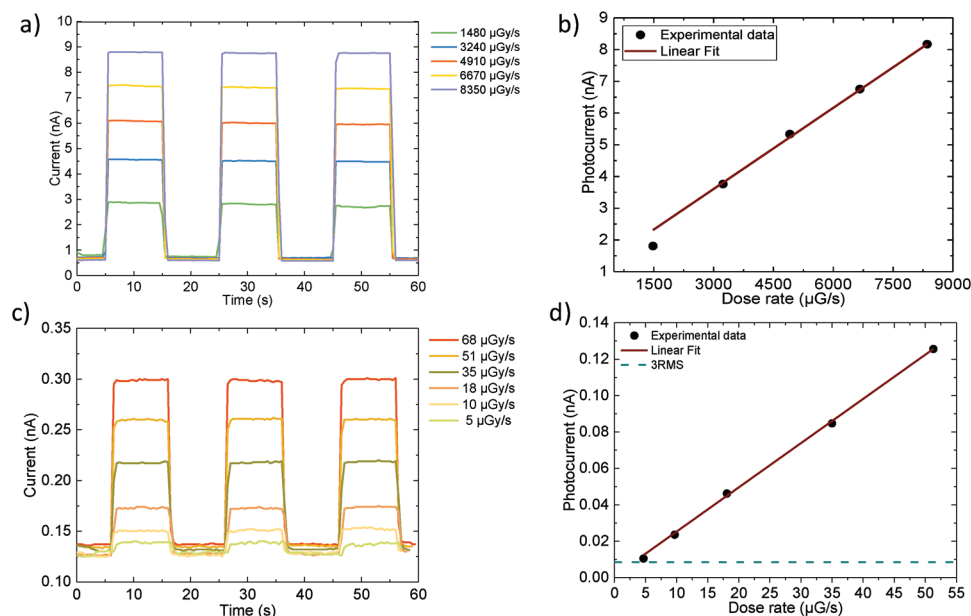


**Figure 5.** a) Response of a 50 wt.% perovskite content device when exposed to pulsed 150 kVp photons at different doses. b) Photocurrent versus dose rate of the results in (a), where a linear fit is applied. c) Response of a 50 wt.% perovskite content device when exposed to pulsed 150 kVp photons at low doses. d) Photocurrent versus dose rate of the results in (c), where a linear fit is applied and the 3RMS is calculated with a value of 8.43 pA.

Overall, the results of the 50 wt.% perovskite content disks show promising properties for their use as X-ray absorber materials.

### 3. Conclusion

In summary, a dry process to prepare perovskite-polymer composites in ambient air is presented. Mechanochemical synthesized CsPbBr<sub>3</sub> powders are mixed with the polymer PBMA and pressed into thin disks with enhanced mechanical properties. The disks can be handled and laminated on interdigitated ITO/glass substrates, obtaining functional photoconductors. Different perovskite/polymer concentrations were evaluated. The composite containing 75 wt.% of perovskite resulted in the highest specific detectivity with a mean value of  $2 \times 10^{11}$  Jones, at an applied field of  $2.5 \text{ V } \mu\text{m}^{-1}$ . The spectral response of the photoconductors was found to be rather constant over the whole absorption range of the perovskite. Despite the thick composite film and the large inter-electrode distance (40  $\mu\text{m}$ ), a rise time of 1.78 ms is measured for the 75 wt.% devices. Moreover, the thickness of the composite disks can be leveraged to obtain narrow-band detectors, by illuminating the device from the perovskite-polymer material. The peak of the narrow band detector with a thickness of 25  $\mu\text{m}$  is at 555 nm, and with a very narrow FWHM of 15 nm, and a maximum detectivity of  $7 \times 10^9$  Jones. Furthermore, the 50 wt.% perovskite-containing disks have promising properties as X-ray absorbers, as they showed low dark current, linear and fast response, and a detection limit of  $3 \mu\text{G s}^{-1}$ . Overall, this process shows a simplified route to produce polymer-embedded perovskite photodetectors, processed in air and in the absence of solvents. Due to the fabrication's simplicity and the process's flexibility, it can be applied to more complex perovskite systems and applications in real working conditions.

### 4. Experimental Section

**Materials:** Cesium bromide (CsBr, > 99.0%) and lead(II) bromide (PbBr<sub>2</sub>, ≥ 98%) were purchased from TCI. These chemicals were stored in a nitrogen-filled glovebox and used as received without further purification. Poly(butyl methacrylate) was purchased from Sigma-Aldrich and was stored under ambient conditions.

**Materials and Device Preparation:** The CsPbBr<sub>3</sub> perovskite powder was produced by mechanochemical synthesis: the precursor materials (CsBr and PbBr<sub>2</sub>) were introduced in a 1:1 molar ratio and closed inside a 10 mL zirconia ball-mill jar with 2 zirconia beads of 10 mm in diameter. Then ball-milling was performed with an MM-400 straight ball-mill from Retsch, at a frequency of 30 Hz for 5 min, resulting in a CsPbBr<sub>3</sub> perovskite powder. Once the perovskite powder was formed, the polymer was introduced. The mixture was subsequently ball-milled for 3 min, obtaining a homogeneous composite. Disks were prepared in a mold, which was preheated to a temperature of 100 °C, and when the powder was added, a pressure of 2 metric tons was applied. By adjusting the spacer rings, different thicknesses could be achieved. Once the disks were produced, they could be laminated on the desired substrate. Here, a glass substrate with an interdigitated ITO layout was used with 28 ITO contacts with each a spacing of 40  $\mu\text{m}$  and a length of 4960  $\mu\text{m}$ . If needed, the disks could be cut into a desired shape to have a better fit with the substrate. The disks were laminated with a 420 W hot/cold laminator at a temperature of 100 °C.

**XRD Characterization:** X-ray diffraction was measured with a Panalytical Empyrean diffractometer equipped with CuK $\alpha$  anode operated at 45 kV and 40 mA and a Pixel 1D detector in scanning line mode. Single scans

were acquired in the  $2\theta = 10^\circ$  to  $50^\circ$  range in Bragg-Brentano geometry in air.

**Optical characterization:** The PL measurement is performed using a 405 nm matchbox laser where the signal is measured by an Avantes AvaSpec-2048L spectrometer. The reflectance of the disks was measured using the Avantes AvaLight DH-S-BAL deuterium halogen source connected with an Avantes reflection integrating sphere and collected by the Avantes AvaSpec-2048L spectrometer.

**EQE Measurements:** The EQE measurements were measured by exciting the devices with a Quartz Tungsten Halogen lamp connected by a monochromator from Newport. The monochromatic light gets chopped by a chopper which is synchronized with a lock-in amplifier. In this way, the dark current is subtracted and the pure photocurrent can be measured.

**Photo-Response:** The photo response was measured by modulating a Matchbox 405 nm laser with a 1 Hz signal generated by a function generator. The 1 Hz pulsed laser was directed on the device and the output signal of the device was measured by an oscilloscope.

**X-ray Characterization:** The X-ray source was a Hamamatsu L12161 Microfocus X-ray tube with a tungsten (W) target operated at an accelerating voltage of 150 kVp and with filament currents ranging from 10 to 500  $\mu\text{A}$ . The photocurrent was acquired using a Keithley 2614B Precision Source/Measure Unit. During all the irradiation measurements, the sample was kept in a nitrogen atmosphere. X-ray pulse duration was 10 s with a frequency of 0.5 Hz.

### Supporting Information

Supporting Information is available from the Wiley Online Library or from the author.

### Acknowledgements

The authors gratefully acknowledge the financial support of the European Research Council (ERC) under the European Union's Horizon 2020 Research and Innovation Programme (Grant Agreement No. 834431). The authors acknowledge funding from the Ministry of Science and Innovation (MCIN) and the Spanish State Research Agency (AEI) for project PDC2021-121317-100 funded by MCIN/AEI/10.13039/501100011033 and by the "European Union NextGenerationEU/PRTR", and from the Comunitat Valenciana (CISEJ/2022/43). C.B. acknowledges the funding by the EU – NextGenerationEU with funds made available by the National Recovery and Resilience Plan (NRRP) Mission 4, Component 1, Investment 4.1 (MD 351/2022)—NRRP Research.

### Conflict of Interest

The authors declare no conflict of interest.

### Data Availability Statement

The data that support the findings of this study are available from the corresponding author upon reasonable request.

### Keywords

mechanochemical synthesis, narrowband detectors, perovskite photodetectors, solvent-free, X-ray detectors

Received: July 29, 2023

Revised: September 6, 2023

Published online: September 22, 2023

- [1] D. Yang, D. Ma, *Adv. Opt. Mater.* **2019**, 7, 679.
- [2] L. Li, S. Ye, J. Qu, F. Zhou, J. Song, G. Shen, *Small* **2021**, 17, 2005606.
- [3] Z. Zhao, C. Xu, L. Niu, X. Zhang, F. Zhang, *Laser Photonics Rev.* **2020**, 14, 2000262.
- [4] L. Li, S. Ye, J. Qu, F. Zhou, J. Song, G. Shen, *Small* **2021**, 17, 2005606.
- [5] R. Dong, Y. Fang, J. Chae, J. Dai, Z. Xiao, Q. Dong, Y. Yuan, A. Centrone, X. C. Zeng, J. Huang, *Adv. Mater.* **2015**, 27, 1912.
- [6] S. Donati, *Meas. Sci. Technol.* **2001**, 12, 653.
- [7] C. C. Stoumpos, M. G. Kanatzidis, *Acc. Chem. Res.* **2015**, 48, 2791.
- [8] S. D. Stranks, H. J. Snaith, *Nat. Nanotechnol.* **2015**, 10, 391.
- [9] J. S. Manser, M. I. Saidaminov, J. A. Christians, O. M. Bakr, P. V. Kamat, *Acc. Chem. Res.* **2016**, 49, 330.
- [10] F. Wang, X. Zou, M. Xu, H. Wang, H. Wang, H. Guo, J. Guo, P. Wang, M. Peng, Z. Wang, Y. Wang, J. Miao, F. Chen, J. Wang, X. Chen, A. Pan, C. Shan, L. Liao, W. Hu, *Adv. Sci.* **2021**, 8, 2100569.
- [11] Y. Zhang, Y. Ma, Y. Wang, X. Zhang, C. Zuo, L. Shen, L. Ding, *Adv. Mater.* **2021**, 33, 2006691.
- [12] J. Miao, F. Zhang, *J. Mater. Chem. C* **2019**, 7, 1741.
- [13] M. Ahmadi, T. Wu, B. Hu, *Adv. Mater.* **2017**, 29, 1605242.
- [14] N. Leupold, F. Panzer, N. Leupold, F. Panzer, *Adv. Funct. Mater.* **2021**, 31, 2007350.
- [15] F. Palazon, Y. El Ajjouri, H. J. Bolink, *Adv. Energy Mater.* **2020**, 10, 1902499.
- [16] D. Prochowicz, M. Saski, P. Yadav, M. Grätzel, J. Lewiński, *Acc. Chem. Res.* **2019**, 52, 3233.
- [17] L. Martínez-Sarti, F. Palazon, M. Sessolo, H. J. Bolink, *Adv. Opt. Mater.* **2020**, 8, 1901494.
- [18] P. Sadhukhan, S. Kundu, A. Roy, A. Ray, P. Maji, H. Dutta, S. K. Pradhan, S. Das, *Cryst. Growth Des.* **2018**, 18, 3428.
- [19] L. Wang, D. Ma, C. Guo, X. Jiang, M. Li, T. Xu, J. Zhu, B. Fan, W. Liu, G. Shao, H. Xu, H. Wang, R. Zhang, H. Lu, *Appl. Surf. Sci.* **2021**, 543, 148782.
- [20] D. Prochowicz, P. Yadav, M. Saliba, M. Saski, S. M. Zakeeruddin, J. L. Lewiński, M. Grä, *ACS Appl. Mater. Interfaces* **2017**, 9, 28418.
- [21] E. Breniaux, E. J. Marin-Bernardez, E. Gallet, P. Dufour, C. Tenaillon, *Mater. Chem. Phys.* **2020**, 247, 122870.
- [22] B. A. Rosales, L. Wei, J. Vela, *J. Solid State Chem.* **2019**, 271, 206.
- [23] G. García-Espejo, D. Rodríguez-Padrón, R. Luque, L. Camacho, G. De Miguel, *Nanoscale* **2019**, 11, 16650.
- [24] B. A. H. Huisman, H. J. Bolink, *Adv. Opt. Mater.* **2023**, 11, 2202921.
- [25] C. Li, Y. Ma, Y. Xiao, L. Shen, L. Ding, *InfoMat* **2020**, 2, 1247.
- [26] A. Perveen, S. Hussain, Y. Xu, A. Raza, F. Saeed, N. Din, A. Subramanian, Q. Khan, W. Lei, *J. Photochem. Photobiol., A* **2022**, 426, 113764.
- [27] U. Bansode, A. Rahman, S. Ogale, *J. Mater. Chem. C* **2019**, 7, 6986.
- [28] F. Palazon, Y. El Ajjouri, P. Sebastia-Luna, S. Lauciello, L. Manna, H. J. Bolink, *J. Mater. Chem. C* **2019**, 7, 11406.
- [29] C. Li, Z. Zang, C. Han, Z. Hu, X. Tang, J. Du, Y. Leng, K. Sun, *Nano Energy* **2017**, 40, 195.
- [30] M. Rodová, J. Brožek, K. Knížek, K. Nitsch, *J. Therm. Anal. Calorim.* **2003**, 71, 667.
- [31] D. Yang, D. Huo, *J. Mater. Chem. C* **2020**, 8, 6640.
- [32] Y. Zhang, J. Du, X. Wu, G. Zhang, Y. Chu, D. Liu, Y. Zhao, Z. Liang, J. Huang, *ACS Appl. Mater. Interfaces* **2015**, 7, 22.
- [33] C. C. Stoumpos, C. D. Malliakas, J. A. Peters, Z. Liu, M. Sebastian, J. Im, T. C. Chasapis, A. C. Wibowo, D. Y. Chung, A. J. Freeman, B. W. Wessels, M. G. Kanatzidis, *Cryst. Growth Des.* **2013**, 13, 2722.
- [34] X. Hu, X. Zhang, L. Liang, J. Bao, S. Li, W. Yang, Y. Xie, X. Hu, X. Zhang, L. Liang, J. Bao, S. Li, W. Yang, Y. Xie, *Adv. Funct. Mater.* **2014**, 24, 7373.
- [35] A. A. Khan, Z. Yu, U. Khan, L. Dong, *Nanoscale Res. Lett.* **2018**, 13, 399.
- [36] Y. Li, Z. F. Shi, S. Li, L. Z. Lei, H. F. Ji, D. Wu, T. T. Xu, Y. T. Tian, X. J. Li, *J. Mater. Chem. C* **2017**, 5, 8355.
- [37] X. Zhang, F. Li, R. Bai, Q. Sun, Y. Hao, S. Xi, M. Zhu, S. Jiang, W. Jie, Y. Xu, *J. Mater. Chem. C* **2022**, 10, 6017.
- [38] M. I. Saidaminov, M. A. Haque, M. Savoie, A. L. Abdelhady, N. Cho, I. Dursun, U. Buttner, E. Alarousu, T. Wu, O. M. Bakr, *Adv. Mater.* **2016**, 28, 8144.
- [39] Y. Fang, Q. Dong, Y. Shao, Y. Yuan, J. Huang, *Nat. Photonics* **2015**, 9, 679.